Modelling and Simulation in Materials Science and Engineering

PAPER

Predicting microstructure evolution for friction stir extrusion using a cellular automaton method

IOP Publishing Modelling and Simulation in Materials Science and Engineering
Modelling Simul. Mater. Sci. Eng. **27** (2019) 035006 (23pp) https://doi.org/10.1088/1361-651X/ab044b

Predicting microstructure evolution for friction stir extrusion using a cellular automaton method

Reza Abdi Behnagh[1], Avik Samanta[2], Mohsen Agha Mohammad Pour[1], Peyman Esmailzadeh[1] and Hongtao Ding[2]

[1] Faculty of Mechanical Engineering, Urmia University of Technology, Urmia, Iran
[2] Department of Mechanical Engineering, University of Iowa, Iowa City, United States of America

E-mail: hongtao-ding@uiowa.edu

Received 7 November 2018, revised 24 January 2019
Accepted for publication 4 February 2019
Published 6 March 2019

Abstract

Friction stir extrusion (FSE) offers a solid-phase synthesis method consolidating discrete metal chips or powders into bulk material form. In this study, an FSE machine tool with a central hole is driven at high rotational speed into the metal chips contained in a chamber, mechanically stirs and consolidates the work material. The softened consolidated material is extruded through the center hole of the tool, during which material microstructure undergoes significant transformation due to the intensive thermomechanical loadings. Discontinuous dynamic recrystallization is found to have played as the primary mechanism for microstructure evolution of pure magnesium chips during the FSE process. The complex thermomechanical loading during the process drives the microstructure evolution. A three-dimensional finite element process model is developed using commercial software DEFORM 11.0 to predict the thermal field, mechanical deformation and material flow during the FSE process. Using the simulated thermomechanical loadings as input, a cellular automaton model is developed to simulate the dynamic evolution of the material grain microstructure. The predicted grain size is in good agreement with the experimentally measured grain size. This numerical study provides a powerful analysis tool to simulate the microstructure transformation for friction stir-based processes.

Keywords: friction stir extrusion, cellular automaton, finite element model, microstructure evolution, dynamic recrystallization, magnesium

(Some figures may appear in colour only in the online journal)

1. Introduction

Friction stir extrusion (FSE) is a mechanical deformation-based, solid-state recycling process utilizing the principle of friction stir processing [1–6]. The recycling of metal chips is important for society to meet the goals of waste management, pollution control, and reduction of greenhouse gas emission [7, 8]. The conventional method of recycling by melting scraps and chips leads to significant energy consumption. On the other hand, metal chips can be compressed and deformed plastically in non-conventional recycling methods with less energy consumption and without a requirement of subsequent operation for finish product [9–12]. During the FSE process, the chips are kept in a cylindrical container, and a specially designed rotating tool with scrolled face and inner extrusion channel is inserted in the container. A schematic representation of the FSE process and different components required for the process are shown in figure 1. There is intense frictional interaction between the tool and the chips that deforms the material at high strain rate. At the same time, frictional heat raises the temperature of the material as well. In the process, the chips are solid-bonded and undergo a backward extrusion through the extrusion channel in the tool.

Mechanical properties in terms of tensile strength and hardness and quality in terms of surface crack and microstructure of the friction stir extruded wire have been experimentally investigated for FSE process. Behnagh *et al* [1] produced defect-free wire from AA7277 chips using FSE process. They showed that temperature was an important parameter and has a dominating influence on quality of the extruded wire. Hot surface cracks and cold surface tears were observed on the produced wire if the process temperature was too high and too low respectively. Tang and Reynolds [2] observed the same trend of surface crack and tear for their experiments with AA2050 and AA2195 aluminum alloy chips. They observed good ductility and relatively uniform hardness on the friction stir extruded wires. Tahmasbi and Mahmoodi [3] performed a compression test on the extruded wires and found that with increasing tool rotational speed during the FSE process, hardness and yield strength of the extruded wire were reduced. On the other hand, increasing the extrusion force to a certain extent led to increase in yield stress of the material. They also showed that increased tool rotational speed led to reduced dislocation density in the extruded wires. Material flow behavior during the FSE process is also an important aspect that influences the quality of the extruded part. Recently, FSE process is used to produce defect-free Al-SiC metal matrix composite by introducing SiC powders with AA2024 chips during the process [13].

It is important to develop numerical models to capture the process mechanics and material flow pattern for better comprehension of the process. Zhang *et al* [14] used computational fluid dynamics to simulate the complex flow of material by considering the material as non-Newtonian fluid with temperature and strain rate dependent viscosity. They observed that a helical material flow induced by tool rotation and traverse occurred in the extruded part. They predicted the velocity field, particle path lines, strain rates, viscosity distribution, and the deformation region. 3D Lagrangian, thermo-mechanically coupled finite element (FE) model was also developed to capture temperature distribution and material flow path during the process [5].

Substantial microstructural change has been observed experimentally during the FSE process of aluminum alloys [1–3] and magnesium alloys [4–6]. As the FSE process included complex thermomechanical loading that incorporated plastic deformation, strong frictional interaction at the tool-workpiece interface, it is essential to understand the mechanism of microstructure evolution during the process to foresee the mechanical performance of the extruded part. Dynamic recrystallization (DRX) is the most dominating mechanism of microstructure evolution during friction stir processes [15–18]. Researchers have

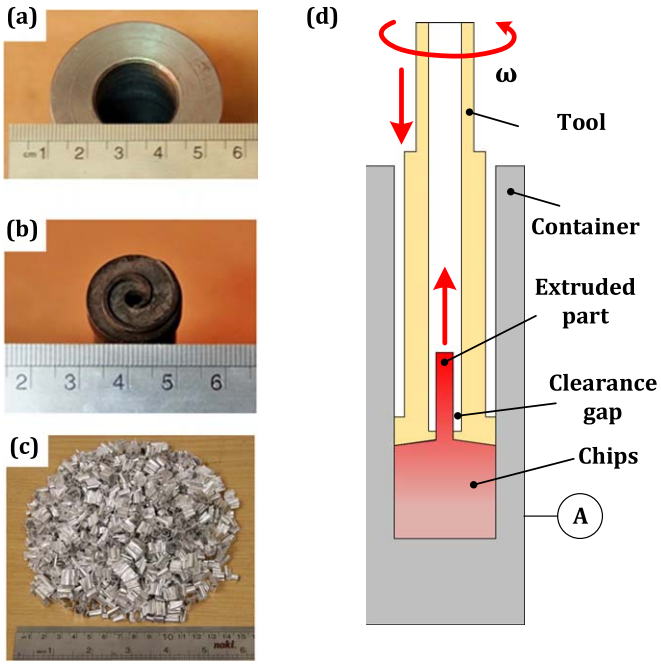

Figure 1. Experimental setup for the FSE process; (a) the container; (b) the tool with scrolled face and central hole; (c) machined magnesium chips; and (d) schematic of the process.

experimentally observed that plastic deformation at high temperature leading to DRX induced microstructure in the extruded material [1–3, 6]. Tool rotational speed and plunge rate exerted significant influence on the formation of the final microstructure of the extruded part as they contributed to the deformation rate and heat generation. Multistep metallo-thermo-mechanically coupled Eulerian–Lagrangian FE model with DRX kinetics has been developed to predict the evolution of microstructure during the FSE process [6]. The model predicted the distribution of DRXed grain size and the microhardness. However, the dynamic microstructure evolution by DRX in terms of nucleation and thermally driven grain growth is beyond the scope of the FE model.

Cellular automaton (CA) method is capable of capturing the dynamic evolution of microstructure under complex thermomechanical loading of hot forming processes [19, 20]. The microstructure evolution of steels [20–23], magnesium alloys [24, 25], copper [19, 26, 27], and titanium alloy [28] governed by DRX has been simulated by CA method in last few years. It has been widely acknowledged that it is a powerful numerical methodology to simulate the DRX dominated evolution of microstructure with computational efficiency. However, these CA models mainly simulated process with constant temperatures and low strain rates. On the contrary, FSE process is a high strain rate problem with gradient strain rate from edge to center of the extruded part, which makes it a challenging problem to model the microstructure evolution. In recent years, authors have developed a CA-based microstructure model [29] to simulate DRX governed microstructure evolution of the friction stir blind riveting process of aluminum alloy. Gradient microstructure was simulated at the tool-workpiece interface and validated against experimental results.

Table 1. Materials and experimental conditions for FSE.

Processed alloy	Pure Mg
Tool material	H13 tool steel
Tool rotational velocity (rpm)	180, 250, 355
Tool plunge rate (mm min^{-1})	14
Extrusion hole diameter (mm)	5

In this paper, a comprehensive analysis of the mechanism of DRX governed evolution of microstructure is discussed for the FSE process of magnesium. A three-dimensional (3D) FE process model is developed to simulate the thermomechanical response during FSE process. Finally, for the first time, a two-dimensional (2D) CA-based microstructure evolution model is established to simulate the DRX dominated microstructure transformation of work material undergoing the FSE process. The thermomechanical response predicted by the FE model is fed into the CA model as loading condition. The CA model consists of multiple mechanisms including dislocation accumulation during plastic deformation, dynamic recovery, DRX, and temperature driven grain growth kinetics. A comprehensive analysis is conducted to understand how processing parameter affects the microstructure evolution. FSE experiments were performed to validate the process model and microstructure evolution.

2. Principles of microstructure evolution during FSE

2.1. Experimental analysis

The schematic representation of the FSE process with main components is shown in figure 1. The setup consists of three main components, i.e. the container, a tool with a scrolled face and the magnesium chips as shown in figures 1(a)–(c). Dry and pure magnesium chips were produced by machining a magnesium ingot using a planning machine in dry condition. The container was filled with the magnesium chips. The rotating tool was driven into the container at a constant speed. The stirring action of the tool created friction between tool and chip, which deformed the work material and generated frictional heat. As a result, a solid wire was extruded through the channel inside the tool. The temperature of all the components increased during the process. The temperature on the extrusion container wall was recorded using an infrared thermometer. Tool material and process parameters used in the experiments are listed in table 1.

Optical microscopy (OM) images of the magnesium ingot and the chips used in the FSE process are illustrated in figures 2(a) and (b). As-received pure magnesium ingot had uniformly distributed coarse grains of about 800 μm. The machined chips which were produced by machining the ingot had an average grain size of 13.5 μm. The extruded wire was sectioned perpendicular to the extrusion direction to investigate the microstructure. The samples were polished and etched following the ASTM standards [30, 31]. In the beginning, 1000-grit Al_2O_3 paper, with 1 μm diameter diamond paste was used to polish the specimens followed by polishing with silica paste with particle size of 40 nm. Post polishing, Acetic-Picral etchant (5 ml Acetic Acid, 6 g Picric Acid, 100 ml Ethanol, and 10 ml Water) was used to etch the polished surface to prepare it for microstructure measurement. Optical micrographs were taken at the center, middle and edge of the cross-section area of the extruded wire using OLYMPUS PMG3 OM. From figure 2, significant grain refinement was observed from the

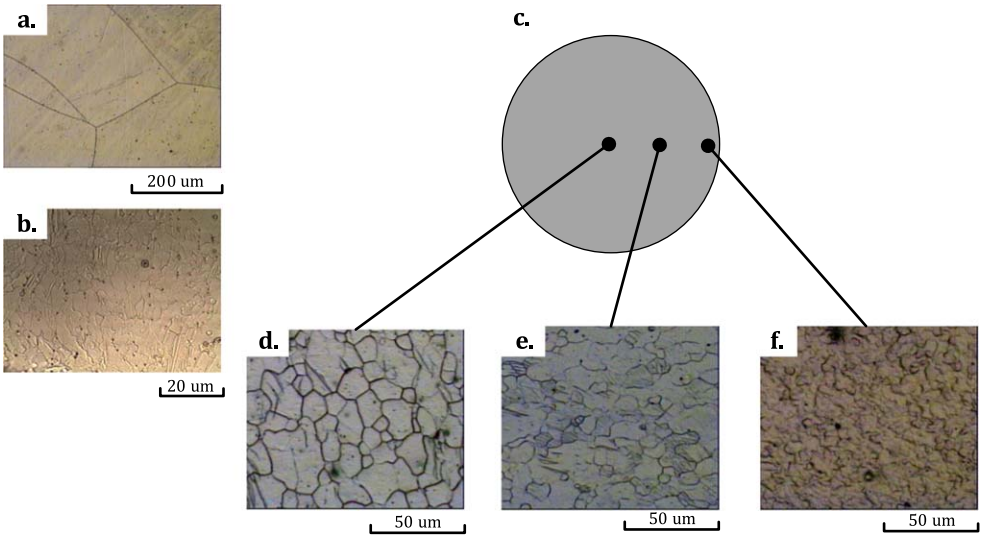

Figure 2. Experimental analysis of microstructure: (a) magnesium ingot; (b) machined chips; (c) illustration of cross-section area; grain structure (d) at the center; (e) at the middle and (f) at the edge.

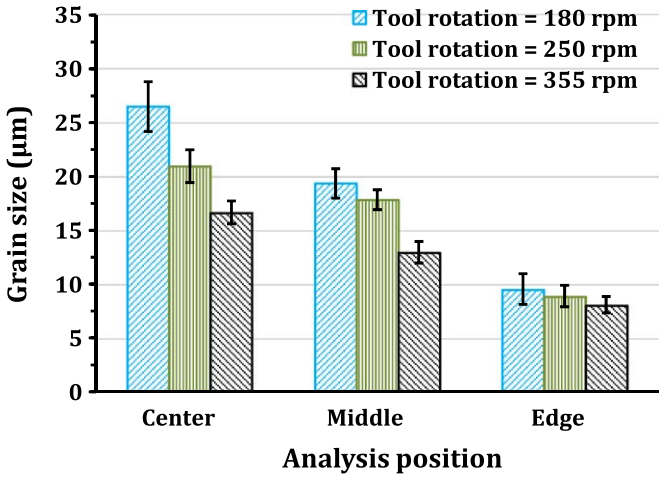

Figure 3. Average grain size distribution from the center to edge of the friction stir extruded part.

center to edge of the friction stir extruded part. The grain size was measured from the micrograph using open source MATLAB program 'linecut.' Average grain size was 5–8 μm at the edge whereas near the center area it was around 15–20 μm in size (figures 3(d)–(f)).

2.2. Mechanisms of microstructure evolution during FSE

Intense work material and tool interaction is one of the prime features of friction stir processes and both sliding and sticking friction contribute to the deformation of the work material [32, 33]. The material around the tool experiences stirring effect which deforms the work

material. Unlike other hot metallurgical deformation processes, friction stir processes are high strain rate processes where strain rate is heavily influenced by tool rotational speed [34–36]. The friction between the rotating tool and work material also generate a lot of heat during the process, which takes the process temperature beyond the recrystallization point of the work material [36–38]. High temperature plastic deformation means the material has conserved enough strain energy to trigger DRX [6, 29, 39, 40].

Three main DRX mechanisms are reported for engineering metals and their alloys, i.e. continuous dynamic recrystallization (cDRX) [41–43], discontinuous dynamic recrystallization (dDRX) [44–47] and geometric dynamic recrystallization (gDRX) [46, 48, 49]. During cDRX, dislocation buildup and increase of misorientation between subgrains led to form new grains. On the contrary, for dDRX, high accumulation of dislocations led the formation of new grains on the grain boundaries followed by migration of the high-angle grain boundaries (HABs) [41, 44]. On the other hand, subgrain boundary formation within a grain and dynamic recovery at high-temperatures and low strain rates for some materials created new grains by gDRX [49]. The stacking fault energy (SFE) is one of the key factors that decide the mechanism of DRX. High SFE metals, such as aluminum alloys, ferritic steels, and alpha titanium alloys are more prone to endure cDRX rather than dDRX at plastic deformation in high temperature. On the other hand, low to medium SFE metals, such as beta titanium alloys, austenitic steels, and magnesium alloys, trend to experience dDRX rather than cDRX for similar thermos-mechanical loading condition [41, 42, 50]. Strain rate is another key factor that contributes to the mechanism of DRX [48, 51]. It has been observed that cDRX is dominating mechanism when the strain rate of the deformed region is low whereas dDRX is dominating when the strain rate is high [48]. Magnesium and its alloys show the occurrence of both cDRX and dDRX for hot deformation processes [18, 52–54], but friction stir processes predominantly induce dDRX. Both Yuan *et al* [55] and Chang *et al* [56, 57] indicates that due to high strain rate during friction stir processes, microstructural defects are generated in the workpiece which is favorable for dDRX nucleation. Fatemi-Varzaneh *et al* [54] suggest that both temperature range and strain rate play influential roles to decide the DRX mechanism of AZ31 magnesium alloy. If the temperature is above 450 °C and the strain rate is above 0.1 s–1, dDRX dominates the recrystallization process.

During the FSE process, a high-speed rotating tool approaches the magnesium chips in the container, the chips around the tool undergo stirring which leads to plastic deformation of the work material. High strain and strain rate exist at the outside of the extruded wire whereas material away from the edge experiences less strain and strain rate. The extruded part has different grain size distribution from edge to center as shown in figure 2. Based on the thermomechanical conditions of the extruded part, the optical micrographs at a different location and prior research done on magnesium and its alloys, the work material in FSE process undergoes dDRX which predominantly influence the microstructure evolution during the process.

3. Finite element process modeling

A 3D thermomechanical model was developed using a commercial FE software package of DEFORM 11.0, a Lagrangian implicit code designed for metal forming processes, to simulate the thermomechanical process response during the FSE process and subsequent cooling process. The deformation and thermal history were simulated simultaneously. The thermomechanical

Table 2. Thermo-physical properties for pure Mg [6, 59].

Property	Value
Density (kg m^{-3})	1741.6–0.1369 · T ($T \leqslant 650$ °C)
Young's modulus (GPa)	44.104–0.0242 · T ($T \leqslant 350$ °C)
	35 ($350 \leqslant T \leqslant 650$ °C)
Poisson's ratio	0.35
Melting point (°C)	650
Thermal conductivity (W m^{-1} °C)	418
Specific heat (J kg^{-1} °C)	1009.6 + 0.5305 · T ($T \leqslant 650$ °C)
Thermal expansion (μm m^{-1} °C)	25.2

Table 3. JC model parameters for pure Mg [60].

A (MPa)	B (MPa)	n_{JC}	C	m_{JC}	T_r (°C)	$\dot{\varepsilon}_o$ (1/s)
153	291.8	0.1026	0.013	1.5	20	1

responses were fed into the subsequent CA microstructure evolution model to simulate the dynamic microstructure change during the FSE process.

According to experiments, the FSE process can be divided into two main stages. First stage was to consolidate the Mg chips inside the container and convert them into a billet with continuous material. Second stage was the extrusion of the wire. In this step material extruded from the top surface into the extruded wire. One of the most critical aspects of the FSE simulation was the material modeling for the magnesium chips. It should be noted that the chips were discrete and there were voids or pores in between the chips. It is very complicated and computationally expensive to model individual chips and the frictional interaction between them. It has been shown by researchers that the chips were compacted inside the extrusion container and porosity reduced to zero before the beginning of the extrusion process as a result of the deformation and material stirring of the tool [58]. Consequently, it is assumed that all the chips inside the container were a single object. As an initial condition of the FE simulation, the magnesium chips are already compacted and considered as a single object. So, the properties of continuous magnesium are used for the simulation.

Table 2 lists the temperature-dependent thermal and physical properties of pure magnesium which are used in the FE model. The flow stress behavior of the work material was modeled using Johnson–Cook (JC) constitutive model. JC model defined the material flow stress as a function of strain, strain rate, and temperature during the process simulation

$$\bar{\sigma} = (A + B\varepsilon^{n_{JC}})\left[1 + C\ln\left(\frac{\dot{\varepsilon}}{\dot{\varepsilon}_0}\right)\right]\left(1 - \left(\frac{T - T_r}{T_m - T_r}\right)^{m_{JC}}\right), \quad (1)$$

where ε denoted the equivalent plastic strain; $\dot{\varepsilon}$ represented the equivalent plastic strain rate; T was the temperature, A, B, n_{JC}, m_{JC}, $\dot{\varepsilon}_o$ and C are material parameters; T_m and T_r were the melting and room temperature respectively. The material parameters used in the JC model were listed in table 3.

In this FE model, only second stage of the process was simulated, but, it should be noted that the temperature has risen to some extent during the first stage of compaction of chips [4]. In this present work, the chips were assumed to be a single solid material, and the effect of

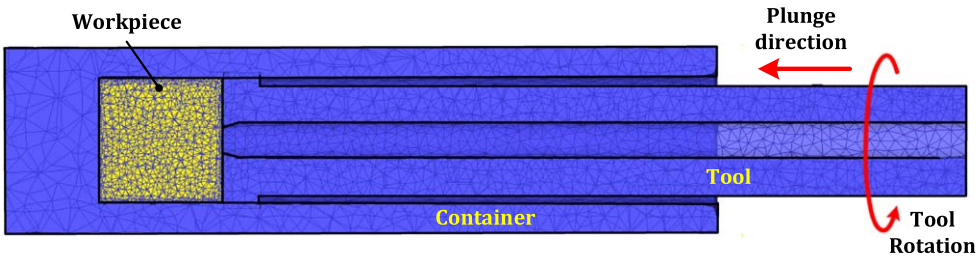

Figure 4. FE modeling setup for FSE process.

compaction stage at the process was considered by applying the preheating temperature to the billet. A preheating temperature of 200 °C was applied to the billet prior to the start of FSE process simulation as a similar temperature was observed from previous experimental work [4].

Figure 4 shows the cross-section of the modeling configuration for the FSE process in DEFORM 11.0. Both of tool and the container were considered as rigid bodies, and the extrusion container was fixed in all direction. The tool was provided with a rotational motion about the longitudinal axis and a linear plunge rate towards the workpiece billet as shown in figure 4.

A clearance was provided between the inner hole of the rotating tool and the extruded wire to avert additional frictional obstruction and to reduce power consumption during the process. The tool, extrusion container and workpiece were meshed with tetrahedral elements. Multiple simulations were conducted with varying tool rotational speed from 180 to 355 rpm and a constant plunge rate of 14 mm min^{-1}. A uniform shear friction was considered between tool-billet and billet-container interface. A friction factor of 0.57 was used at those frictional interfaces [61] and the heat transfer coefficient was assumed as 10 W m^{-2} K^{-1} in the frictional interface. After the FSE process simulation, the tool was disconnected from the simulation system, and the workpiece was cooled using a natural convection (20 W m^{-2} K) condition.

4. CA modeling of microstructure evolution

A 2D DRX model based on CA method was developed for the FSE process for the first time considering the complex thermomechanical loading, dDRX, and grain growth kinetics. The CA model was built on the evolution of dislocation density. The evolution of dislocation density was modeled based on the authors' previous work [29] for the aluminum alloy for the friction stir blind riveting process. The commencement of DRX at high temperature was modeled using the critical dislocation density approach [19, 20, 24, 28, 62]. The dislocation density evolution model was combined with the DRX nucleation model and thermally driven grain growth kinetics model adopted from Ding and Guo [62]. Microstructural evolution during FSE process of magnesium chips was simulated using the CA model developed in MATLAB. As explained earlier, the FSE process imposed plastic deformation on the work material, and friction between tool and workpiece increased the temperature very close to material recrystallization temperature. The strain rate and temperature simulated in the FE based process model was fed into the CA model as loading conditions. The microstructure evolution was captured based on this loading condition following a given set of evolution

laws. The CA model developed in this research can simulate the evolution of grains in the cross-sectional plane of the extruded wire. The main rationale behind the development of the CA model was to capture the gradient microstructure in the radial direction as observed in the experimental analysis. As the model was 2D in nature, it was unable to capture the evolution of microstructure in the extrusion direction.

It was assumed that the initial crystal structure was defect-free with uniform dislocation density and no grain rotation. DRX was assumed to take place when the dislocation density of a particular grain reached a critical value determined by thermomechanical loading conditions, i.e. strain rate and temperature [62, 63]. The grain boundary energy and dislocation energy were considered as the two main driving force for DRX. The elastic strain energy and surface energy were assumed to have no effect on the driving force for recrystallization. As discussed in section 2.2, dDRX was established as the mechanism of recrystallization for the FSE process. Hence, DRX nucleation was assumed to take place only on grain boundaries that included both primary grain boundaries and DRX grain boundaries. This assumption agreed to the grain boundary bulging nucleation mechanism of dDRX of Magnesium, which was supported by many experimental observations [54–57].

4.1. Dislocation evolution laws, DRX nucleation, and grain growth kinetics

During plastic deformation, dislocations were gathered in the deformed grains leading to work hardening. At the same time, dislocation annihilation led to dynamic recovery. When the resultant dislocation density reached a critical value, DRX took place and new grains were nucleated and the dislocation density was reset. All these three competing mechanisms contributed to the evolution of dislocation density during any process with plastic deformation. Kocks and Mecking model proposed by [64, 65] combined work hardening and dynamic recovery to calculate the change of dislocation density of a cell.

$$\frac{\partial \rho_{i,j}}{\partial \varepsilon} = k_1 \sqrt{\rho_{i,j}} - k_2 \rho_{i,j}, \tag{2}$$

where $\rho_{i,j}$ was the dislocation density of a cell at location *i, j;* ε was the strain; k_1 and k_2 were material constants. The value of k_1 and k_2 can be determined from stress-strain data. k_1 remained constant for different strain rate and temperature whereas k_2 was a strong function of strain rate and temperature [66]. k_2 can be expressed as:

$$k_2 = A_1 \left(\dot{\varepsilon} \exp\left(-\frac{Q_v}{RT} \right) \right)^n, \tag{3}$$

where A_1, Q_v, n were material parameters; $\dot{\varepsilon}$ is the strain rate; R is the gas constant and T is the temperature in Kelvin scale.

Average dislocation density (ρ_{mean}) was calculated over the domain at each simulation step

$$\rho_{\text{mean}} = \frac{1}{N} \sum_{i,j} \rho_{i,j}, \tag{4}$$

where N is the total number of cell in the simulation domain. The flow stress (σ) was calculated at each step as expressed in [23]:

$$\sigma = \alpha G b \sqrt{\rho_{\text{mean}}}, \tag{5}$$

where α represented the dislocation interaction term which was 0.5 for magnesium; G was the shear modulus, and b is the Burger's vector.

During DRX simulation, the event of DRX nucleation was one of the essential condition which took place when accumulated dislocation density reached a critical value. This critical value depended on the material and thermomechanical deformation condition in terms of temperature and strain rate. When the accumulated dislocation density in a specific grain of the work material attained the critical dislocation density, new nucleus would generate at a random cell along grain boundaries. That critical dislocation density value was calculated by [67]:

$$\rho_{\text{crit}} = \left(\frac{20\gamma_m \dot{\varepsilon}}{3blM_{\text{gb}}\xi^2}\right)^{\frac{1}{3}}, \tag{6}$$

where γ_m denoted the grain boundary energy of high-angle boundary; l represented the dislocation mean free path; M_{gb} stood for the grain boundary mobility; and ξ was the dislocation line energy. They were calculated by [51, 66, 68]:

$$\gamma_m = \frac{Gb\theta_m}{4\pi(1-\nu)}, \tag{7}$$

$$l = \frac{c_1 Gb}{\sigma}, \tag{8}$$

$$M_{\text{gb}} = \dot{\varepsilon}\frac{\delta D_{0b} b}{KT}\exp\left(-\frac{Q_b}{RT}\right), \tag{9}$$

$$\xi = c_2 Gb^2, \tag{10}$$

where θ_m stood for HAB, it was considered as $\pi/12$ radian; ν was the Poisson's ratio; δ denoted the grain boundary thickness; D_{0b} represented the grain boundary self-diffusion coefficient at 0 K; K denoted the Boltzmann constant, Q_b was the grain boundary diffusion activation energy; R stood for the ideal gas constant; and c_1 and c_2 were material parameters.

The nucleation rate $\dot{n}(\dot{\varepsilon}, T)$ per unit grain boundary was modeled as a function of strain rate [69] and temperature [63] and it is expressed as:

$$\dot{n}(\dot{\varepsilon}, T) = c_3 \dot{\varepsilon}^m \exp\left(-\frac{Q_{\text{act}}}{RT}\right), \tag{11}$$

where Q_{act} denoted the activation energy; and c_3 and m were material parameters.

The dislocation density of the new DRX nuclei was set to ρ_{initial} which was a small number very close to zero. The difference in dislocation density between the newly recrystallized grains and the matrix worked as the driving force for the growth of new DRX nuclei. The grain boundary moved from recrystallized grains towards the matrix grains as matrix grains had higher dislocation density compared to recrystallized grains. The grain growth rate can be calculated by:

$$V_i = M_{\text{gb}} f_i, \tag{12}$$

where f_i denoted the driving force per unit area that contributed to the evolution of recrystallized grains, which is given by:

$$f_i = \tau(\rho_m - \rho_i) - 2\frac{\gamma_i}{d_i}, \tag{13}$$

where ρ_m stood for total dislocation density of matrix grains; ρ_i represented the total dislocation density recrystallized grains, respectively; d_i was the diameter of DRXed grain,

and γ_i was the grain boundary energy of the DRXed grain. γ_i was determined by the equation proposed by Read–Shockley [70],

$$\gamma_i = \begin{cases} \gamma_m \dfrac{\theta_i}{\theta_m}\left[1 - \ln\left(\dfrac{\theta_i}{\theta_m}\right)\right] & for \quad \theta_i \leqslant \theta_m \\ \gamma_m & for \quad \theta_i > \theta_m \end{cases}, \tag{14}$$

where θ_i denoted the difference in orientation between grains i that has undergone DRX, and it is adjacent grains.

All the parameters discussed above for the development of the CA model for microstructure evolution of Magnesium were listed in table 4.

4.2. CA model formulation

The 2D CA model code was written in MATLAB combining dislocation density evolution model, DRX nucleation model and grain growth kinetics model along with CA transformation rules. The simulation domain consisted of equally spaced CA cells that evolved during the simulation based on the loading condition and transformation rules. Each CA cell had six variables that attributed to six physical parameters that control the state of the cell during the simulation. Those six variables included (1) orientation of grain, (2) the label of grain boundary, (3) total dislocation density, (4) the label of recrystallized grains, (5) index of recrystallization, and (6) index of color. The CA cells evolved depending on the status of neighboring cell according to the 2D von Neumann's nearest neighboring rule. The initial microstructure of the simulation domain was constructed by a grain growth algorithm. Randomly distributed nuclei were set inside the domain, and those nuclei grew until the whole domain was covered. Subsequently, actual CA simulation was performed based on the thermomechanical loading from the FE model.

During the simulation, the dislocation density of each cell ($\rho_{i,j}$) was updated continuously at each time step based on the thermomechanical loading obtained from the FE simulations. When the dislocation density went beyond critical dislocation density, a random distribution of DRX nucleus was introduced along the grain boundary based on a probabilistic transformation rule. In each step, DRX nucleation probability, P_{nuc} was calculated according to the following equation:

$$P_{\text{nuc}} = \dot{n} \times \Delta t \times S_{\text{CA}}, \tag{15}$$

where Δt denoted the time increment in CA simulation; S_{CA} represented the area of a CA cell. As the current model assumed square CA cells, $S_{\text{CA}} = L_{\text{CA}}^2$, where L_{CA} was the length of the cell.

A random number P between 1 and 0 was generated and assigned to cells on the grain boundary. The value of P was compared with P_{nuc} in each step. If $P < P_{\text{nuc}}$ condition was satisfied, the cell was turned into a DRX nucleus. The state variables of that particular cell were updated as well. Otherwise, the cell remained in the original grain and the value of the state variables remained the same.

The newly created DRX nucleus was subjected to further evolution and growth based on the thermomechanical loading, and the grain boundary migrated accordingly. The migration distance (L_G) of grain boundary was calculated by:

$$L_G = V_i \Delta t. \tag{16}$$

Table 4. CA model parameters [66, 71–73].

Variable	k_1	A	Q_v (kJ mol^{-1})	n	b (nm)	G (GPa)	θ_m (rad)	ν	c_1
Value	2.66×10^9	660.17	129.913	−0.119	0.321	17	$\pi/12$	0.35	10
Variable	δD_{0b} (m^3 s^{-1})	K (m^2 kg s^{-2} K^{-1})	Q_b (kJ mol^{-1})	R (J.mol^{-1} K^{-1})	c_2	c_3	m	Q_{act} (kJ mol^{-1})	
Value	5.92×10^{-12}	1.38×10^{-23}	109	8.314	0.5	4.493×10^{10}	0.848	157	

Table 5. Details of CA simulations.

Simulation	Location	Simulation domain (μm^2)	L_{CA} (μm)
1	Center	250 × 250	1
2	Middle	250 × 250	1
3	Edge	125 × 125	0.5

The size of a particular recrystallized grain (r) was calculated by [23]:

$$r = \sqrt{N_{DRX} \times \frac{S_{CA}}{\pi}}, \tag{17}$$

where N_{DRX} denoted the total number of the CA cells occupied by this recrystallized grain. When the value of V_i reached to zero, grain growth stopped. To track the progress of DRX, volume fraction of recrystallized grain (X_{DRX}) was calculated by:

$$X_{DRX} = \frac{N_{DRX}}{N_X \times N_Y}, \tag{18}$$

where N_X and N_Y denoted the number of cells in the domain along X- and Y-axis respectively.

The radius of the extruded wire was 2.5 mm which was significantly large considering the computational cost. So, three separate simulation domains were chosen for the center, middle and edge area of the cross-section. The edge area had shown small grain size as observed from experimental analysis. The thermomechanical loading histories were extracted from the FE simulation conducted in section 3 and fed into the CA simulation. A square shape 2D simulation domain with 250 square cells in each direction was used with a resolution of the domain denoted by L_{CA}. The details of each CA simulation was listed in table 5. The CA simulation consists of two steps, i.e. the deformation process during FSE and subsequent cooling step.

5. Results and discussions

5.1. Finite element process model results

The predicted temperature profiles were compared with the values obtained with the infrared thermometer to verify the simulation results. The temperature of the extruded wire was difficult to measure as it was enclosed by the rotating tool, so the temperature was measured at location A on the container wall as shown in figure 1. Figure 5 showed the comparison of simulated and experimentally measured temperature histories at the container wall. The simulated temperature profiles agreed well with the experimentally measured values. As the rotational speed of the die increased, the peak temperature also increased. The peak temperature was almost 200 °C higher as the tool rotational speed increased from 180 to 355 rpm. The simulated results also followed the same trend as the experimental result. Figure 6 showed the temperature distribution on the extruded wire after 10 s of FSE process simulation. The peak temperature was observed near the neck area near the extrusion hole. Higher rotational speed contributed to the higher rate of friction between work material and tool that resulted in higher frictional heat generation. As the tool rotation speed increased from 180 to 355 rpm, the temperature on the extruded wire increased from 530 °C to 630 °C. The temperature contour was also very uniform in the cross-section of the wire. The temperature on the wire for all rotational speed in this study was higher than 0.8 T_m which was required to

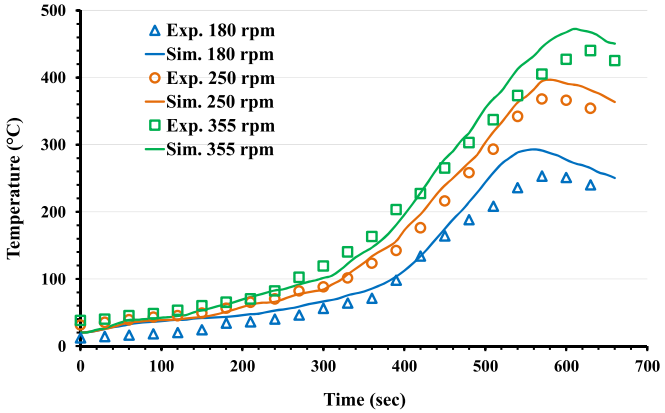

Figure 5. Comparison between predicted temperature and experiments.

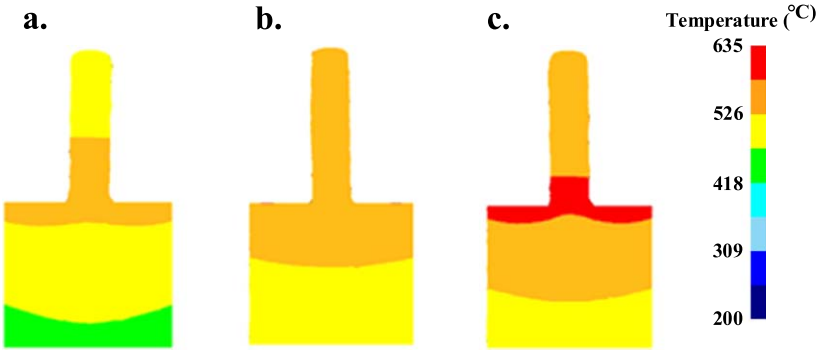

Figure 6. Temperature distribution at different tool rotational speed: (a) 180 (b) 250; (c) 355 rpm.

trigger DRX. There was limited relative movement between container and billet during the extrusion stage. Most of the relative movement was between tool and billet. So, the friction between tool and billet played the major role in heating during the simulation. At this stage, friction between the billet and the container existed, but had no effect on heating due limited relative velocity between billet and container.

The strain distribution on the wire for different rotational speed was shown in figure 7 after 10 s of process simulation. The cross-section was taken at the neck region of the wire and distribution of strain from the center to edge was shown as well. As the tool rotational speed was increased, the strain was also increased. When the tool rotational speed was 180 rpm, most of the area at the wire center had strain value in the range of $2.2 < \text{strain} < 3$. The strain value suddenly increased from 3 to 4.5 near the edge region covering a distance of 1.1 mm (figures 7(a) and (d)). The same trend was followed for higher tool rotational speed for 250 rpm and 355 rpm. The high strain region (strain > 3) increased to 2 mm and 2.5 mm respectively for 250 rpm and 355 rpm tool rotational speed (figures 7(b)–(d)). Higher tool

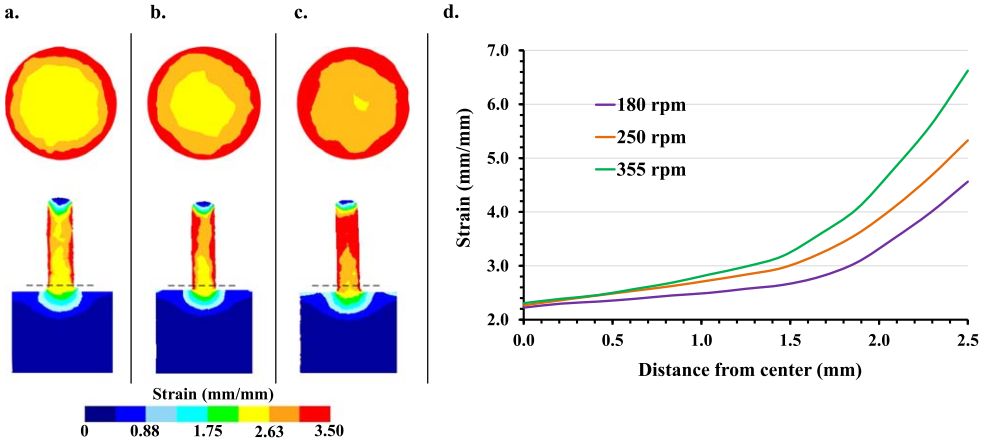

Figure 7. Strain distribution after 10 s of simulation at different tool rotational speed: (a) 180 (b) 250; (c) 355 rpm and (d) strain distribution from the center to the edge of the extruded wire.

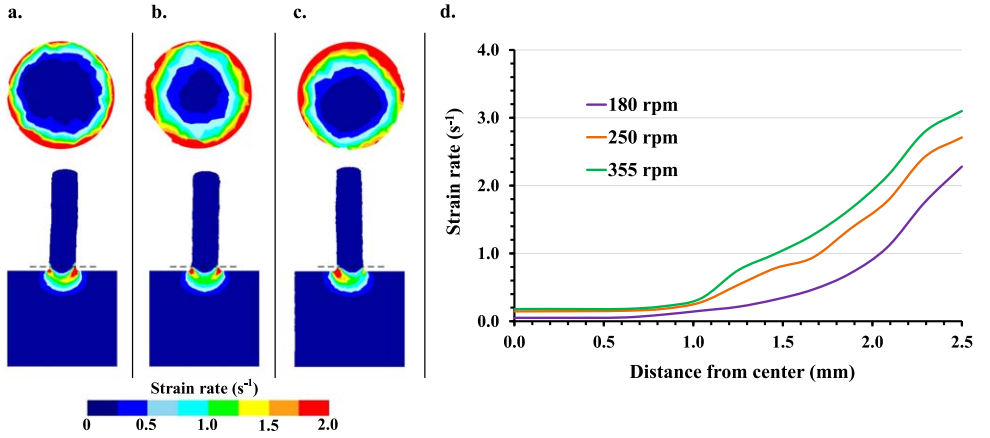

Figure 8. Strain rate distribution after 10 s of simulation at different tool rotational speed: (a) 180 (b) 250; (c) 355 rpm and (d) strain rate distribution from the center to the edge of the extruded wire.

rotational speed stood for more material stirring near the tool surface which led to higher strain depth from the tool surface.

Figure 8 showed the strain rate distribution of the extruded wire for different rotational speed. A cross-section was taken at the neck region of the extruded wire and shown in figures 8(a)–(c) for tool rotational speed of 180 rpm, 250 rpm, and 355 rpm, respectively. As the tool rotational speed increased, the strain rate increased because higher rotational speed led to higher tangential stirring velocity around the tool. As a result, material deformation rate increases leading to a higher strain rate. This trend agreed with other friction stir processes [29, 34]. The strain rate around the tool increased by 45% as the rotational speed increased from 180 to 355 rpm (figure 8(d)).

The material flow had a key role in the formation, structural integrity, and the overall properties of the extruded wires. The material flow in forming processes was usually tracked

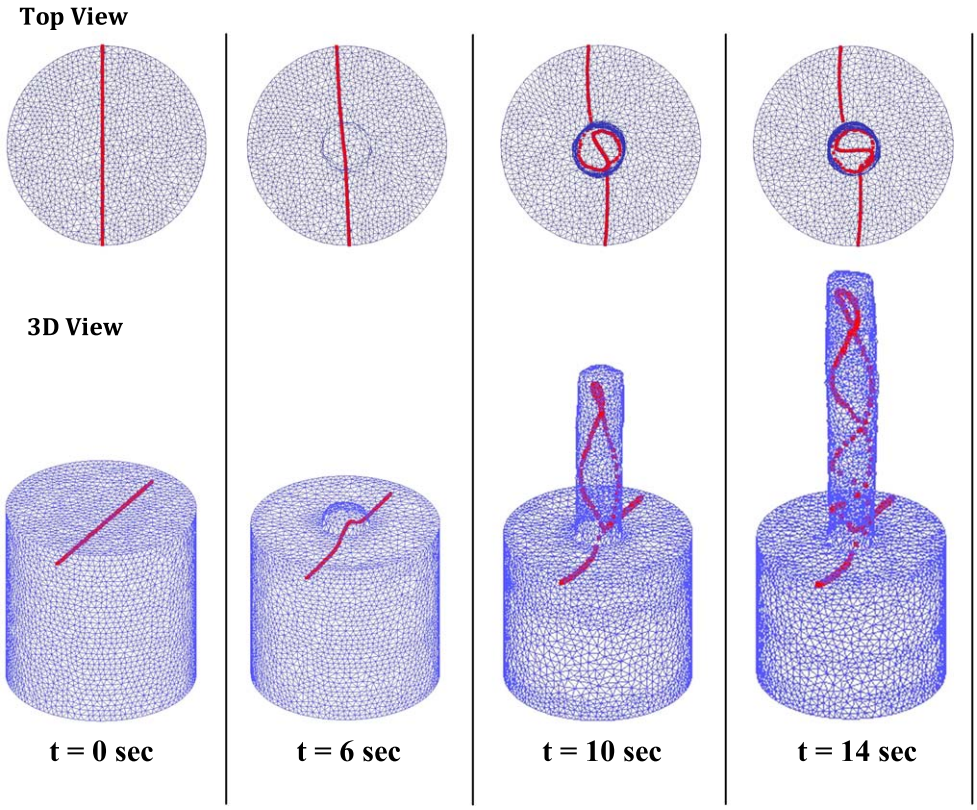

Figure 9. Top view and 3D view of material flow by tracking positions of predefined points at different time step with tool rotation of 355 rpm.

experimentally by applying the so-called marker insert technique. The markers were inserted into the workpiece material, and their final positions after the forming process were discovered using a metallographic study or x-ray radiography. However, this method was very costly and time-consuming. Alternatively, material flow can be tracked by numerical simulation by tracking some specified points before and after the simulation. In this case, a series of point on a straight line is tracked at a depth of 1.5 mm from the surface. Figure 9 showed the evolution of the positions tracking points at different time frames when the tool rotation was 355 rpm. The material was restrained by the rigid rotating tool and the wall of the container. At the beginning of the process, material flowed toward the extrusion hole from the top of consolidate chips, with a defined speed of the feed rate. It can be observed that the movement of the nodes were centrifugal along the thickness direction where they were pulled upwards and rotated simultaneously. The centrifugal movement of the nodes of the extruded wire was due to the axial movement in the feeding direction and rotational movement of the tool happening at the same time. The rotational movement of the tool facilitated the stirring action that induced spiral movement of material along the radial direction, and the axial movement of the tool pulled the spiral upward to make a 3D spiral distribution of the material. The billet material was also involved in rotational movement during the simulation but, the movement was limited compared to the flow inside extruded wire as shown on the top views in figure 9. The tool rotation could not rotate the entire billet during extrusion. It only rotated the material on the surface layer. The billet was almost fixed in the bottom of the container

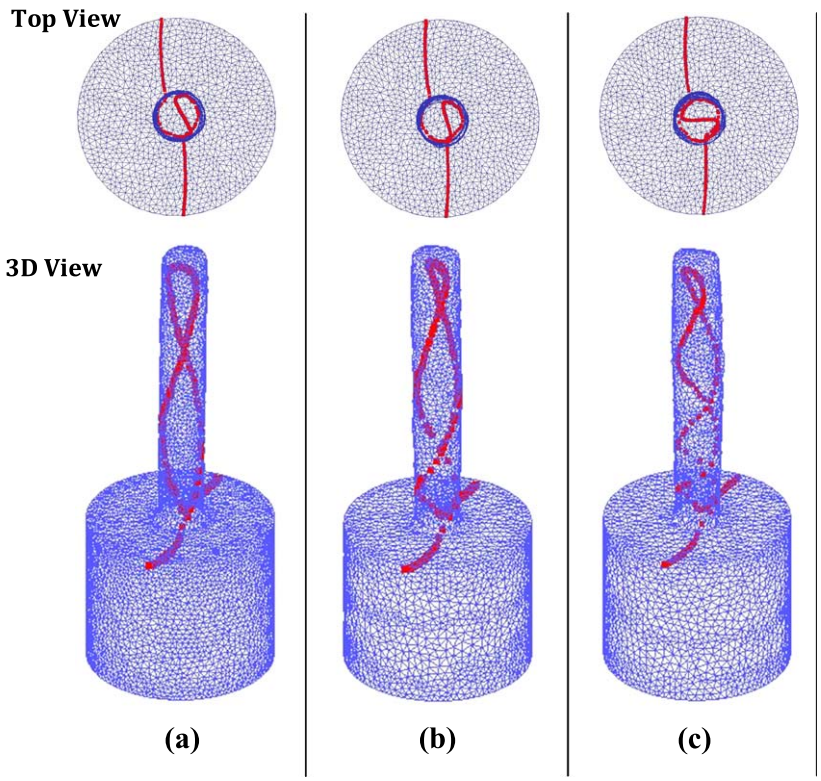

Figure 10. Top view and 3D view of material flow by tracking positions of predefined points at different tool rotational speed: the position of the tracking points after 14 s of simulation for (a) 180; (b) 250 and (c) 355 rpm.

and side of the container due to larger frictional surface. As the simulation progressed, the tracking points came near to the surface and the rotation can be seen. The scrolled face of the rotating tool further facilitated the stirring action and flow of the material into the extrusion hole, but it is not considered in this study.

Figure 10 showed the evolution of the positions of tracking points after 14 s of simulation for different tool rotation conditions. As the tool rotation increased from 180 to 355 rpm, the same material point endured more helical movement. It meant the same material element suffered more strain and strain rate at higher tool rotation. These numerical results agreed well with the reported computational fluid dynamics and experimental work by Zhao *et al* [74].

5.2. Microstructure simulation results

Using the above established 2D CA model, the microstructure evolution of the magnesium undergoing FSE process was simulated. It was assumed that the consolidated chip was annealed during the FSE process and had an initial average grain size of 25 μm. It was considered that a uniform dislocation density of $10^{10}\,\mathrm{m}^{-2}$ existed in the hole domain (typical level of dislocation density for well-annealed magnesium [75, 76]). As the FSE process involved intense frictional interaction between tool and work material, the temperature of the work material was simulated to go beyond $0.8\,T_m$ for triggering the DRX. Previous work suggested that DRX commenced before the consolidated chips go into the die inlet due to

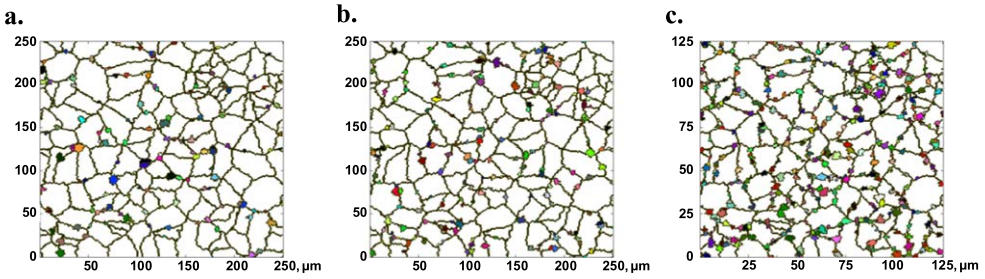

Figure 11. Difference in DRX nucleation at a different location of the cross-section of the extruded wire: (a) at the center; (b) at the middle and (c) at the edge.

high temperature and plastic deformation [6]. As the simulation progressed, the dislocation density was evolved based on the thermomechanical loading condition of the domain. When the condition of accumulated dislocation density of a specific grain became equal or above the critical dislocation density, sporadic DRX nuclei were generated on the grain boundaries as shown in figure 11. The strain and strain rate of the edge area of the extruded wire was significantly higher compared to center area as demonstrated by the FE simulation results. As the value of dislocation density was proportional to strain and strain rate, the dislocation density of edge area increased faster compared to the center area of the extruded wire. It indicated that the edge area grains reached critical dislocation density much faster than center area grains. As a result, more DRX nuclei were generated in edge area compared to center area (figures 11(a)–(c)).

After the material went beyond the neck region, the plastic deformation ceased very quickly, and the extruded wire underwent cooling phase. Therefore, nucleation of new DRX site ceased, and only temperature driven grain growth took place subsequently. As the extruded wire passed through the inside hole of the die, it was not exposed to the environment immediately. As a result, the cooling rate was not as first as other friction stir processes. Consequently, a significant amount of grain growth happened. Figure 12 showed the final simulated microstructure from the CA model and compared them to the experimentally observed microstructures at the center, middle and the edge area of the extruded wire when the tool rotational speed was 250 rpm. The simulated microstructure reasonably agreed with the experimentally observed microstructures. In the center area, the grains (figure 12(d)) were relatively larger compared to the middle and edge area (figures 12(e) and (f)). The center area cooled slower than the edge area which let the center area to have more time for thermal driven grain growth or grain coarsening. At the same time, the edge area had more DRX nuclei that had less space to grow whereas the center area had less DRX nuclei and more space to grow. The simulated microstructures were analyzed using open source MATLAB program 'linecut.' The histogram plot of grain size showed that the percentage of simulated grain sizes matched reasonably well with the experimentally measured values as shown in figures 12(g)–(i).

More CA simulations were conducted with the FE model simulated thermomechanical loading conditions for different tool rotational speed. Figure 13 showed the comparison of simulated average grain size and experimentally measured average grain size. A significant agreement has been found. The CA simulated grain size was under-predicted by 5%–15% compared to experimentally observed values. The source of the error came probably from the fact that the deformed shape of the grains was not included in the current study.

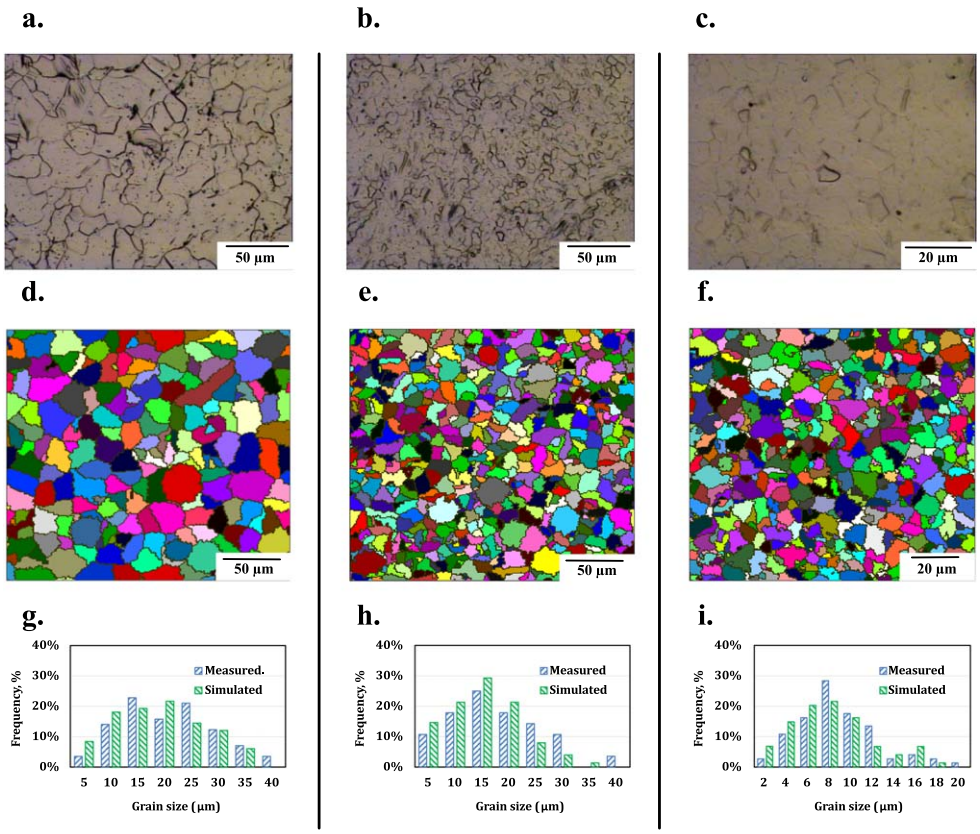

Figure 12. Optical micrographs (a)–(c) and simulated microstructures (d)–(f), and comparison of histograms of experimentally measured and predicted grain size distribution for FSE process with tool rotation 250 rpm for three CA simulations (Sim. 1 at center of the extruded wire, Sim. 2 at mid region along radius of the extruded wire, and Sim. 3 at the edge area of the extruded wire).

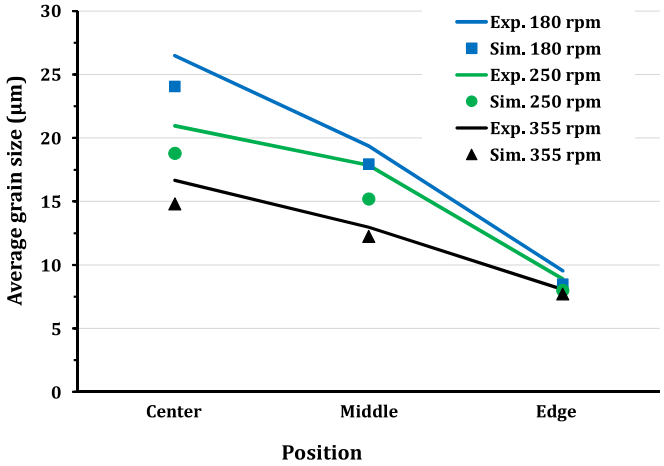

Figure 13. Comparison of simulated and experimentally measured average grain size.

6. Conclusion

In this work, microstructure analysis had been performed on the extruded wire from FSE process of magnesium chips. DRXed microstructure was observed on the cross-section of the extruded wire. Fine and coarse grains were observed on edge and the center of the extruded wire, respectively. dDRX was argued to be the DRX mechanism during the process. A thermomechanical FE element process model was developed to simulate the thermo-mechanical behavior during the process. The FE model was validated against the measured temperature during the experiment.

A MATLAB based CA model was established to simulate microstructure transformation during the FSE process. The microstructure evolution from the center to the edge of the extruded wire was simulated for different tool rotational speed. The dDRX of the grains was modeled based on the dislocation density evolution under thermomechanical loading condition. The simulation results showed that the strain and strain rate distribution across the wire cross-section and process temperature played the principal role for DRX event during the process. The simulated grain size and distribution was in good agreement with the experimentally observed microstructure.

Acknowledgments

The authors gratefully acknowledge the financial support provided for part of the study carried out at the University of Iowa by the National Science Foundation under grant No. CMMI-1537512.

ORCID iDs

Hongtao Ding https://orcid.org/0000-0002-0547-1579

References

[1] Behnagh R A, Mahdavinejad R, Yavari A, Abdollahi M and Narvan M 2014 Production of wire from AA7277 aluminum chips via friction-stir extrusion (FSE) *Metall. Mater. Trans.* B **45** 1484–9
[2] Tang W and Reynolds A P 2010 Production of wire via friction extrusion of aluminum alloy machining chips *J. Mater. Process. Technol.* **210** 2231–7
[3] Tahmasbi K and Mahmoodi M 2018 Evaluation of microstructure and mechanical properties of aluminum AA7022 produced by friction stir extrusion *J. Manuf. Process.* **32** 151–9
[4] Ansari M A, Behnagh R A, Narvan M, Naeini E S, Givi M K B and Ding H 2016 Optimization of friction stir extrusion (FSE) parameters through taguchi technique *Trans. Indian Inst. Met.* **69** 1351–7
[5] Baffari D, Buffa G, Campanella D, Fratini L and Reynolds A P 2017 Process mechanics in friction stir extrusion of magnesium alloys chips through experiments and numerical simulation *J. Manuf. Process.* **29** 41–9
[6] Behnagh R A, Shen N, Ansari M A, Narvan M, Besharati Givi M K and Ding H 2015 Experimental analysis and microstructure modeling of friction stir extrusion of magnesium chips *J. Manuf. Sci. Eng.* **138** 041008
[7] Damgaard A and Christensen T H 2011 *Recycling of Metals Solid Waste Technology & Management* ed T H Christensen (Oxford: Blackwell) pp 234–42
[8] Sun Z, Xiao Y, Agterhuis H, Sietsma J and Yang Y 2016 Recycling of metals from urban mines—a strategic evaluation *J. Clean. Prod.* **112** 2977–87

[9] Ji Z S, Wen L H and Li X L 2009 Mechanical properties and fracture behavior of Mg–2.4Nd–0.6Zn–0.6Zr alloys fabricated by solid recycling process *J. Mater. Process. Technol.* **209** 2128–34
[10] Chino Y, Hoshika T and Mabuchi M 2006 Mechanical and corrosion properties of AZ31 magnesium alloy repeatedly recycled by hot extrusion *Mater. Trans.* **47** 1040–6
[11] Chino Y, Hoshika T and Mabuchi M 2006 Enhanced corrosion properties of pure Mg and AZ31Mg alloy recycled by solid-state process *Mater. Sci. Eng.* A **435–436** 275–81
[12] Ying T, Zheng M, Hu X and Wu K 2010 Recycling of AZ91 Mg alloy through consolidation of machined chips by extrusion and ECAP *Trans. Nonferr. Met. Soc. China* **20** s604–7
[13] Baffari D, Buffa G, Campanella D and Fratini L 2017 Al–SiC metal matrix composite production through friction stir extrusion of aluminum chips *Proc. Eng.* **207** 419–24
[14] Zhang H, Zhao X, Deng X, Sutton M A, Reynolds A P, McNeill S R and Ke X 2014 Investigation of material flow during friction extrusion process *Int. J. Mech. Sci.* **85** 130–41
[15] Jata K V and Semiatin S L 2000 Continuous dynamic recrystallization during friction stir welding of high strength aluminum alloys *Scr. Mater.* **43** 743–9
[16] McNelley T R, Swaminathan S and Su J Q 2008 Recrystallization mechanisms during friction stir welding/processing of aluminum alloys *Scr. Mater.* **58** 349–54
[17] Liu G, Murr L E, Niou C S, McClure J C and Vega F R 1997 Microstructural aspects of the friction-stir welding of 6061-T6 aluminum *Scr. Mater.* **37** 355–61
[18] Mironov S, Onuma T, Sato Y S and Kokawa H 2015 Microstructure evolution during friction-stir welding of AZ31 magnesium alloy *Acta Mater.* **100** 301–12
[19] Kugler G and Turk R 2004 Modeling the dynamic recrystallization under multi-stage hot deformation *Acta Mater.* **52** 4659–68
[20] Zheng C, Xiao N, Li D and Li Y 2008 Microstructure prediction of the austenite recrystallization during multi-pass steel strip hot rolling: a cellular automaton modeling *Comput. Mater. Sci.* **44** 507–14
[21] Chen F, Cui Z, Liu J, Zhang X and Chen W 2009 Modeling and simulation on dynamic recrystallization of 30Cr2Ni4MoV rotor steel using the cellular automaton method *Modelling Simul. Mater. Sci. Eng.* **17** 075015
[22] Chen F, Cui Z, Liu J, Chen W and Chen S 2010 Mesoscale simulation of the high-temperature austenitizing and dynamic recrystallization by coupling a cellular automaton with a topology deformation technique *Mater. Sci. Eng.* A **527** 5539–49
[23] Chen F, Qi K, Cui Z and Lai X 2014 Modeling the dynamic recrystallization in austenitic stainless steel using cellular automaton method *Comput. Mater. Sci.* **83** 331–40
[24] Yin H and Felicelli S D 2009 A cellular automaton model for dendrite growth in magnesium alloy AZ91 *Modelling Simul. Mater. Sci. Eng.* **17** 75011
[25] Ding H, Liu L, Kamado S, Ding W and Kojima Y 2009 Investigation of the hot compression behavior of the Mg–9Al–1Zn alloy using EBSP analysis and a cellular automata simulation *Modelling Simul. Mater. Sci. Eng.* **17** 025009
[26] Xiao N, Zheng C, Li D and Li Y 2008 A simulation of dynamic recrystallization by coupling a cellular automaton method with a topology deformation technique *Comput. Mater. Sci.* **41** 366–74
[27] Hallberg H, Wallin M and Ristinmaa M 2010 Simulation of discontinuous dynamic recrystallization in pure Cu using a probabilistic cellular automaton *Comput. Mater. Sci.* **49** 25–34
[28] Zhang Y, Jiang S, Liang Y and Hu L 2013 Simulation of dynamic recrystallization of NiTi shape memory alloy during hot compression deformation based on cellular automaton *Comput. Mater. Sci.* **71** 124–34
[29] Samanta A, Shen N, Ji H, Wang W, Li J and Ding H 2018 Cellular automaton simulation of microstructure evolution for friction stir blind riveting *J. Manuf. Sci. Eng.* **140** 031016
[30] ASTM E407-07(2015)e1 2015 *Standard practice for microetching metals and alloys* (West Conshocken, PA: ASTM International) (https://doi.org/10.1520/E0407-07R15E01)
[31] ASTM E3-11 2011 *Standard guide for preparation of metallographic specimens* (West Conshohocken, PA: ASTM International) (https://doi.org/10.1520/E0003-11R17)
[32] Mishra R S and Ma Z Y 2005 Friction stir welding and processing *Mater. Sci. Eng.* R **50** 1–78
[33] Ma Z Y 2008 Friction stir processing technology: a review *Metall. Mater. Trans.* A **39** 642–58
[34] Pan W, Li D, Tartakovsky A M, Ahzi S, Khraisheh M and Khaleel M 2013 A new smoothed particle hydrodynamics non-newtonian model for friction stir welding: process modeling and simulation of microstructure evolution in a magnesium alloy *Int. J. Plast.* **48** 189–204

[35] Arora A, Zhang Z, De A and DebRoy T 2009 Strains and strain rates during friction stir welding *Scr. Mater.* **61** 863–6
[36] Schmidt H B and Hattel J H 2008 Thermal modelling of friction stir welding *Scr. Mater.* **58** 332–7
[37] Nandan R, Roy G G, Lienert T J and Debroy T 2007 Three-dimensional heat and material flow during friction stir welding of mild steel *Acta Mater.* **55** 883–95
[38] Sidhar H, Martinez N Y, Mishra R S and Silvanus J 2016 Friction stir welding of Al–Mg–Li 1424 alloy *Mater. Des.* **106** 146–52
[39] Shen N, Samanta A, Ding H and Cai W W 2016 Simulating microstructure evolution of battery tabs during ultrasonic welding *J. Manuf. Process.* **23** 306–14
[40] Shen N, Samanta A and Ding H 2017 Microstructure simulations for orthogonal cutting via a cellular automaton model *Proc. CIRP* **58** 543–8
[41] Sakai T and Jonas J J 1984 Dynamic recrystallization: mechanical and microstructural considerations *Acta Metall.* **32** 189–209
[42] Gourdet S and Montheillet F 2003 A model of continuous dynamic recrystallization *Acta Mater.* **51** 2685–99
[43] Bacca M, Hayhurst D R and McMeekingabde R M 2015 Continuous dynamic recrystallization during severe plastic deformation *Mech. Mater.* **90** 148–56
[44] Su J Q, Nelson T W and Sterling C J 2005 Microstructure evolution during FSW/FSP of high strength aluminum alloys *Mater. Sci. Eng.* A **405** 277–86
[45] Rhodes C G, Mahoney M W, Bingel W H and Calabrese M 2003 Fine-grain evolution in friction-stir processed 7050 aluminum *Scr. Mater.* **48** 1451–5
[46] Feng X, Liu H and Suresh Babu S 2011 Effect of grain size refinement and precipitation reactions on strengthening in friction stir processed Al-Cu alloys *Scr. Mater.* **65** 1057–60
[47] Li D, Zhang D, Liu S, Shan Z, Zhang X, Wang Q and Han S 2016 Dynamic recrystallization behavior of 7085 aluminum alloy during hot deformation *Trans. Nonferr. Met. Soc. China* **26** 1491–7
[48] Rokni M R, Zarei-Hanzaki A, Roostaei A A and Abedi H R 2011 An investigation into the hot deformation characteristics of 7075 aluminum alloy *Mater. Des.* **32** 2339–44
[49] Kassner M E and Barrabes S R 2005 New developments in geometric dynamic recrystallization *Mater. Sci. Eng.* A **410–411** 152–5
[50] Guo-zheng Q 2013 Characterization for dynamic recrystallization kinetics based on stress–strain curves *Recent developments in the study of recrystallization* (London: IntechOpen) pp 61–88
[51] Humphreys F J and Hatherly M 2004 *Recrystallization and related annealing phenomena* (Oxford: Pergamon)
[52] Huang Y, Wang Y, Meng X, Wan L, Cao J, Zhou L and Feng J 2017 Dynamic recrystallization and mechanical properties of friction stir processed Mg–Zn–Y–Zr alloys *J. Mater. Process. Technol.* **249** 331–8
[53] Sitdikov O and Kaibyshev R 2001 Dynamic recrystallization in pure magnesium *Mater. Trans. JIM* **42** 1928–37
[54] Fatemi-Varzaneh S M, Zarei-Hanzaki A and Beladi H 2007 Dynamic recrystallization in AZ31 magnesium alloy *Mater. Sci. Eng.* A **456** 52–7
[55] Yuan W, Mishra R S, Carlson B, Verma R and Mishra R K 2012 Material flow and microstructural evolution during friction stir spot welding of AZ31 magnesium alloy *Mater. Sci. Eng.* A **543** 200–9
[56] Chang C I, Du X H and Huang J C 2008 Producing nanograined microstructure in Mg–Al–Zn alloy by two-step friction stir processing *Scr. Mater.* **59** 356–9
[57] Chang C I, Lee C J and Huang J C 2004 Relationship between grain size and zener-holloman parameter during friction stir processing in AZ31 Mg alloys *Scr. Mater.* **51** 509–14
[58] Baffari D, Buffa G and Fratini L 2017 A numerical model for wire integrity prediction in friction stir extrusion of magnesium alloys *J. Mater. Process. Technol.* **247** 1–10
[59] Erickson S C 1990 *Properties of Pure Metals Properties and Selection: Nonferrous Alloys and Special-Purpose Materials* vol 2 (Materials Park, OH: ASM International) pp 1099–201
[60] Liu J 2012 *Experimental Study and Modeling of Mechanical Micro-Machining of Particle Reinforced Heterogeneous Materials* (Orlando, FL: The University of Central Florida)
[61] Kumar K, Kalyan C, Kailas S V and Srivatsan T S 2009 An investigation of friction during friction stir welding of metallic materials *Mater. Manuf. Process.* **24** 438–45
[62] Ding R and Guo Z X 2001 Coupled quantitative simulation of microstructural evolution and plastic flow during dynamic recrystallization *Acta Mater.* **49** 3163–75

[63] Peczak P 1995 A Monte Carlo study of influence of deformation temperature on dynamic recrystallization *Acta Metall. Mater.* **43** 1279–91
[64] Mecking H and Kocks U F 1981 Kinetics of flow and strain-hardening *Acta Metall.* **29** 1865–75
[65] Kocks U F 1976 Laws for work-hardening and low-temperature creep *J. Eng. Mater. Technol.* **98** 76–85
[66] Chen M S, Yuan W Q, Li H, Bin and Zou Z H 2017 Modeling and simulation of dynamic recrystallization behaviors of magnesium alloy AZ31B using cellular automaton method *Comput. Mater. Sci.* **136** 163–72
[67] Roberts W and Ahlblom B 1978 A nucleation criterion for dynamic recrystallization during hot working *Acta Metall.* **26** 801–13
[68] Derby B 1991 The dependence of grain size on stress during dynamic recrystallisation *Acta Metall. Mater.* **39** 955–62
[69] Peczak P and Luton M J 1993 A Monte Carlo study of the influence of dynamic recovery on dynamic recrystallization *Acta Metall. Mater.* **41** 59–71
[70] Read W T and Shockley W 1950 Dislocation models of crystal grain boundaries *Phys. Rev.* **78** 275–89
[71] Akbari M, Asadi P, Givi M B and Zolghadr P 2016 A cellular automaton model for microstructural simulation of friction stir welded AZ91 magnesium alloy *Modelling Simul. Mater. Sci. Eng.* **24** 035012
[72] Guangyin Y, Yangshan S and Wenjiang D 2001 Effects of bismuth and antimony additions on the microstructure and mechanical properties of AZ91 magnesium alloy *Mater. Sci. Eng.* A **308** 38–44
[73] Wang L, Fang G and Qian L 2018 Modeling of dynamic recrystallization of magnesium alloy using cellular automata considering initial topology of grains *Mater. Sci. Eng.* A **711** 268–83
[74] Zhao X, Sutton M A, Zhang H, Deng X, Reynolds A P, Ke X and Schreier H W 2015 Stereo image based motion measurements in fluids: experimental validation and application in friction extrusion *Exp. Mech.* **55** 177–200
[75] Williamson G K and Smallman R E 1956 III. Dislocation densities in some annealed and cold-worked metals from measurements on the x-ray debye–scherrer spectrum *Phil. Mag.* **1** 34–46
[76] Máthis K, Nyilas K, Axt A, Dragomir-Cernatescu I, Ungár T and Lukáč P 2004 The evolution of non-basal dislocations as a function of deformation temperature in pure magnesium determined by x-ray diffraction *Acta Mater.* **52** 2889–94